Effects of Spatial Scale Modification on the Responses of Surface Wind Stress to the Thermal Front in the Northern South China Sea

RUI SHI,[a,b,c] XINYU GUO,[d] JU CHEN,[a] LILI ZENG,[a,c] BO WU,[b] AND DONGXIAO WANG[e]

[a] *State Key Laboratory of Tropical Oceanography, South China Sea Institute of Oceanology, Chinese Academy of Sciences, Guangzhou, China*
[b] *State Key Laboratory of Numerical Modeling for Atmospheric Sciences and Geophysical Fluid Dynamics, Institute of Atmospheric Physics, Chinese Academy of Sciences, Beijing, China*
[c] *Southern Marine Science and Engineering Guangdong Laboratory (Guangzhou), Guangzhou, China*
[d] *Center for Marine Environmental Studies, Ehime University, Matsuyama, Japan*
[e] *School of Marine Sciences, Sun Yat-Sen University, Guangzhou, China*

(Manuscript received 30 June 2021, in final form 7 October 2021)

ABSTRACT: The responses of surface wind stress to the mesoscale sea surface temperature (SST) anomalies associated with the SST front in the northern South China Sea (NSCS) are studied using satellite observations and reanalysis data. Both satellite and reanalysis data explicitly show the linear relationships between the spatial-high-pass filtered wind stress perturbation derivatives and the underlying SST gradient field. However, the noise in the linear relationships is much smaller in the reanalysis data than in the satellite observations. This result is rarely reported in other frontal areas. The wavelet analysis shows that the satellite scatterometer observed numerous high wavenumber perturbations within 100 km in the NSCS, but these perturbations were absent in the reanalysis data. The linear relationship between the perturbation SST gradient and derivative wind stress fields is not significant at this scale, which enhances the noise in the linear relationship. The spatial bandpass-filtered perturbation between 100 and 300 km can give reasonable estimates of the coupling coefficients between the wind stress divergence and downwind SST gradient (α_d) and between the wind stress curl and crosswind SST gradient (α_c) in the NSCS, with values of 1.33×10^{-2} and 0.95×10^{-2} N m^{-2} °C^{-1}, respectively.

SIGNIFICANCE STATEMENT: We examined the responses of surface wind stress divergence and curl to the sea surface temperature front in the northern South China Sea (NSCS) using satellite data and reanalysis products. Satellite observations show significant noise in the linear relationships between surface wind stress derivatives and the sea surface temperature gradient. This result is rarely reported in the frontal areas. We demonstrated that satellite-observed perturbations with specific high wavenumbers are the primary source of such noise. Appropriate bandpass filtering is proposed to depress the noise and provide reasonable air–sea coupling features in the NSCS. An accurate calculation of the coupling features is fundamental for the future study of the interannual variability.

KEYWORDS: Atmosphere; Ocean; Asia; Continental shelf/slope; Sea/ocean surface; Atmosphere-ocean interaction; Fronts; Mesoscale processes; Sea surface temperature; Wind; Air-sea interaction; Coastal meteorology; Satellite observations

1. Introduction

The thermal front is a mesoscale oceanic phenomenon identified by a discontinuity in water temperature in the ocean or at the surface. A sea surface temperature (SST) front is the most commonly observed thermal front in the open ocean and coastal seas. The SST anomalies associated with a front can significantly modify the surface heat fluxes, wind stress, and marine atmospheric boundary layer (MABL) (Chelton and Xie 2010; Shao et al. 2019). Many observations and numerical simulations have identified a positive correlation between surface wind intensity and SST mesoscale anomalies. The surface wind intensity is enhanced when passing across a front from cold to warm water but is reduced when passing from warm to cold water. The linear fitted relationship between the surface wind intensity and mesoscale SST variability is defined as positive SST–wind coupling (Small et al. 2008).

Positive SST–wind coupling is widely confirmed in the frontal area of the eastern tropical Pacific (Chelton et al. 2001), the Kuroshio and its extension (Tokinaga et al. 2006), the Gulf Stream (Minobe et al. 2008), and the Southern Ocean (Byrne et al. 2015). Additionally, the SST-induced response of the surface wind leads to a proportional relationship between the derivative of wind stress and SST gradient components. The surface wind stress divergence ($\nabla \cdot \boldsymbol{\tau}$) and curl ($\nabla \times \boldsymbol{\tau}$) $\cdot$ **k** are linearly related to the downwind and crosswind components of the SST gradient, respectively. The downwind SST gradient can be presented by the vector dot product $\nabla T \cdot \hat{\boldsymbol{\tau}} = |\nabla T| \cos\theta$, and the crosswind SST gradient is presented by the vector cross product $\nabla T \times \hat{\boldsymbol{\tau}} \cdot \mathbf{k} = |\nabla T| \sin\theta$. Here, T is SST, $\hat{\boldsymbol{\tau}}$ is a unit vector in the direction of surface wind stress $\boldsymbol{\tau}$, **k** is the vertical unit vector, and θ is the counterclockwise angle from the vector ∇T to $\boldsymbol{\tau}$ (Chelton et al. 2001; O'Neill et al. 2010a; Oerder et al. 2016).

Denotes content that is immediately available upon publication as open access.

Corresponding author: Rui Shi, shirui@scsio.ac.cn

DOI: 10.1175/JCLI-D-21-0498.1

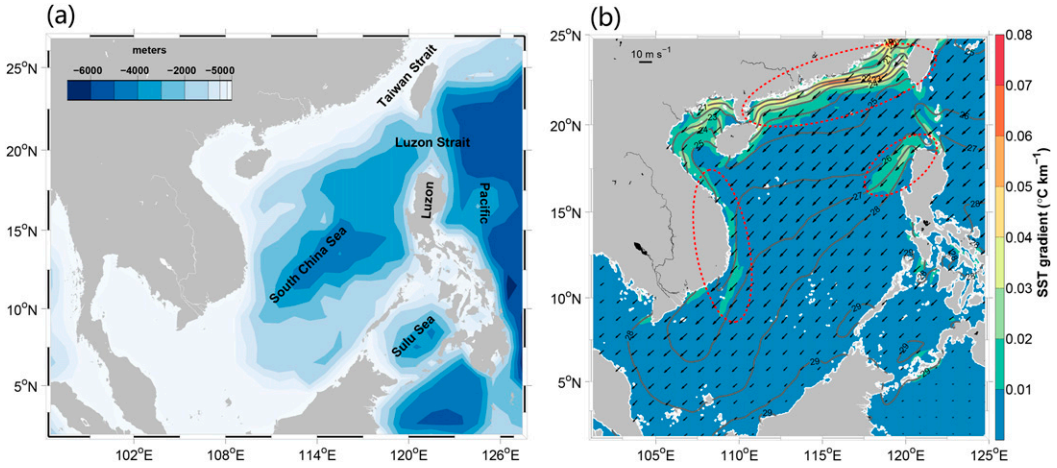

FIG. 1. (a) Map of the SCS and surrounding area; shading shows bathymetry. (b) Monthly mean SST gradient (color shading; °C km^{-1}), SST (gray contours; °C), and sea surface wind (black vectors; m s^{-1}) averaged for December from 2000 to 2019. Three main front systems are marked by the red dashed auxiliary lines.

O'Neill et al. (2010a) clarify that the linear responses of surface wind stress to mesoscale SST variability are mainly attributable to a dynamic response of the actual surface wind. Therefore, the surface wind stress convergence can be directly related to the mass convergence that modifies the vertical motion of the atmosphere. For example, SST-induced mass convergence and vertical motion can have a deep atmospheric response in the form of convective systems and rainfall, which shapes the regional climate in strong western boundary current frontal areas (Minobe et al. 2008; Nakamura et al. 2012; Kuwano-Yoshida and Minobe 2017; O'Neill et al. 2017; Skyllingstad et al. 2019) and coastal front areas (Toy and Johnson 2014; Shi et al. 2019). Furthermore, the SST–wind coupling feedback also affects the fine structures of ocean fronts through Ekman pumping created by mesoscale anomalies in the wind stress curl (Spall 2007; Seo et al. 2007; Perlin et al. 2014; Gaube et al. 2015).

As reviewed by Byrne et al. (2015), various hypotheses have been proposed to explain the adjustment of the sea surface wind field to the SST gradients associated with oceanic fronts. The generation of hydrostatic pressure gradients through adjustments of the MABL mass fields (Lindzen and Nigam 1987) and the stability-dependent modification of the vertical mixing of momentum from aloft to the surface (Wallace et al. 1989; Hayes et al. 1989) are the two major hypotheses. These two mechanisms have also been shown to act together (O'Neill et al. 2010b; Koseki and Watanabe 2010). In addition to these two mechanisms, there are other explanations for the positive SST–wind coupling (Samelson et al. 2006; Skyllingstad et al. 2007). Building upon these findings, O'Neill et al. (2010b) concluded that several regional factors might affect the physical mechanism involved in mesoscale SST–wind coupling. Therefore, mesoscale ocean–atmosphere coupling complicates marginal and coastal seas and still needs to be further studied (Boé et al. 2011; Oerder et al. 2016).

The South China Sea (SCS) is an epicontinental marginal sea strongly influenced by the East Asian monsoon (Fig. 1a). The interaction among the monsoon, bathymetry, and tides generates several kinds of fronts in the coastal sea of the northern SCS (NSCS), especially in winter (Wang et al. 2001; Chu and Wang 2003; Liu et al. 2010; Hu and Wang 2016). During winter, three unique frontal systems are confirmed in the NSCS, off western Luzon, and off eastern Vietnam (Fig. 1b). The NSCS front produces the most dramatic SST gradient among the three frontal systems and has the broadest coverage area in the SCS. It is the focus of this study.

The responses of the surface wind to the mesoscale SST anomalies associated with the NSCS front have been investigated in some previous studies (Chow and Liu 2012; Wang et al. 2012; Shi et al. 2015). The main findings of these previous studies are consistent with the mesoscale SST–wind coupling theory in the open ocean. However, beyond what is known about the wind speed response to mesoscale SST perturbations, little is known about the coupling features between the surface wind stress curl and divergence and such SST anomalies. Furthermore, different coupling coefficients between the surface wind speed and mesoscale SST anomalies are obtained from satellite observations and numerical simulations, and the mechanisms for such differences are still unclear (Shi et al. 2015).

On the other hand, a recent study found that the spatial and preserving time scales of SST perturbations due to the baroclinic instability of the front could be extremely small in the NSCS (Dong and Zhong 2020). These small SST and wind stress perturbations are usually not resolved in the reanalysis data but rather by scatterometers on satellites. The influence of these small-scale SST perturbations on SST–wind coupling is still poorly constrained. Therefore, in this paper we will not further discuss the complicated details of the physical mechanisms but will focus instead on the statistical characteristics of the relationships between the derivative of surface wind stress and SST anomalies at different scales in the NSCS.

In this study, two kinds of surface wind stress and SST data are obtained from satellite observations and ERA5 reanalysis data, as discussed in section 2. The statistical responses of spatial-high-pass filtered surface wind stress divergence and vorticity to crosswind and downwind SST gradients are shown

in section 3. In section 4, the sensitivity experiments show the interference of specific high-wavenumber perturbations on the linear relationships between the derivative wind stress fields and the SST gradient components. An optimal bandpass filter is given in section 4, and corrected coupling coefficients of the SST–wind coupling are proposed for the NSCS. Section 5 gives a brief review of this study.

2. Data and methods

a. Satellite observation and reanalysis data

The sea surface wind data observed by a Quick Scatterometer (QuikSCAT) and Advanced Scatterometer (ASCAT) are used in this study. QuikSCAT data provide extensive geographical and temporal coverage (two times in one day) and higher spatial resolution (0.25°) of the ocean vector winds since late 1999. After QuikSCAT finished its mission in October 2009, ASCAT continued to provide global sea surface wind data. Due to the above advantages of the long period of operation, these two kinds of wind data are broadly used to study the mesoscale SST–wind coupling process over the tropical and midlatitude fronts in the Northern Hemisphere and Southern Ocean (O'Neill et al. 2017).

The Operational SST and Sea Ice Analysis (OSTIA) produced by the U.K. Met Office is used in this study. The OSTIA system makes extensive use of multiple satellite retrievals and assimilates in situ observations from the Global Telecommunications System to generate a global daily SST map with 1/20° (~6 km) resolution back to 1980. It is currently used operationally as the model input condition for the latest Integrated Forecast System (IFS) of the European Centre for Medium-Range Weather Forecasts (ECMWF) (Hersbach et al. 2019). OSTIA data have been successfully applied to drive a regional atmosphere model and study the surface wind response to the oceanic front in the NSCS (Shi et al. 2017).

ERA5 is the latest reanalysis dataset officially released by ECMWF in 2019. ERA5 is based on 4D-Var data assimilation using Cycle 41r2 of the IFS operational model at ECMWF in 2016 (Hans et al. 2019). It is the successor of the ERA-Interim reanalysis that started in 2006. Therefore, ERA5 benefits from a decade of developments in model physics, core dynamics, and data assimilation relative to its precursor ERA-Interim. In addition to a significantly enhanced horizontal resolution (31-km grid spacing compared to 80 km for ERA-Interim), ERA5 also features upgraded high-resolution SST data (OSTIA) and provides remarkable improvements in resolving mesoscale SST–wind coupling around midlatitude oceanic fronts (Hirahara et al. 2016). It is expected that ERA5 can also resolve the SST–wind coupling around the coastal fronts in the NSCS.

In this study, the 10-m equivalent neutral stability wind (ENW) provided by ERA5 was used to calculate the wind stress vector directly observed by the satellite scatterometer. The wind stress vector $\boldsymbol{\tau}$ and 10-m ENW vector $\mathbf{v}_{10n}$ are related by $\boldsymbol{\tau} = \rho_a C_d |\mathbf{v}_{10n}| \cdot \mathbf{v}_{10n}$, where ρ_a is air density (1.29 kg m^{-3}) and C_d is the momentum drag coefficient (1.41×10^{-3}). Although the scatterometer data are absorbed in the data assimilation, the ERA5 surface wind fields still have different statistical features due to the constraint of the dynamical frame and the

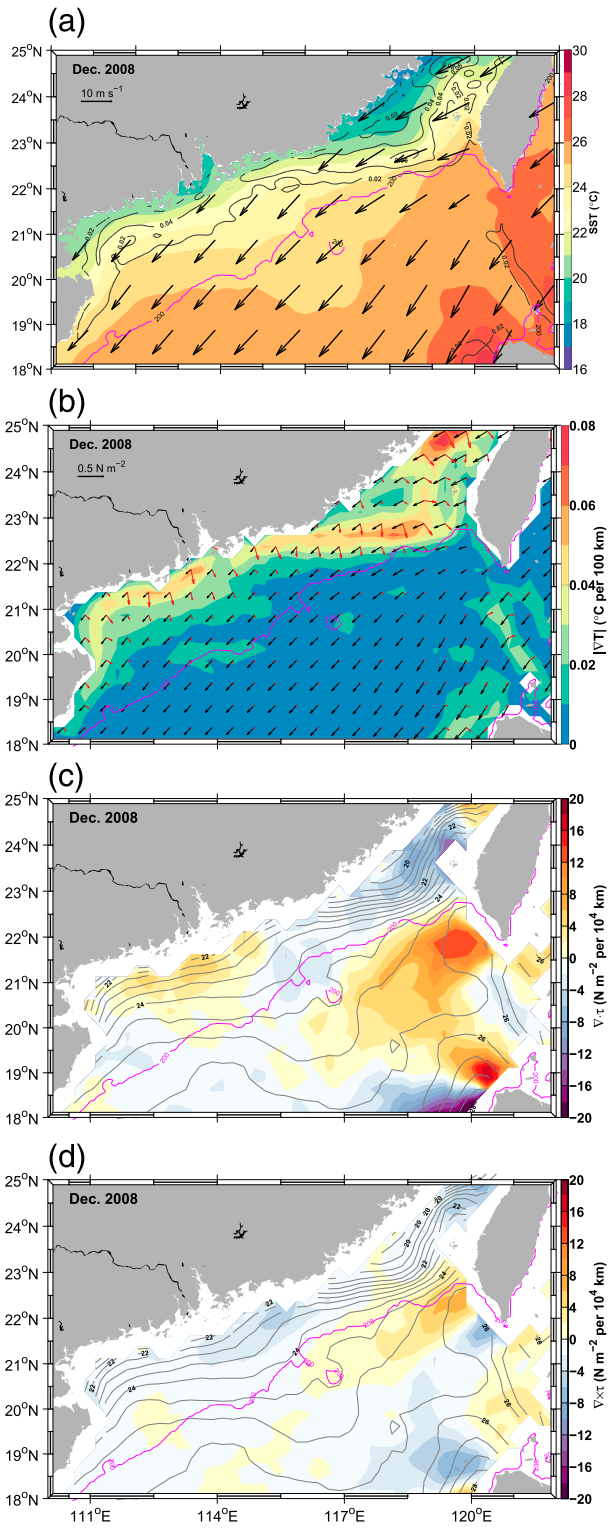

FIG. 2. Monthly average maps in December 2008 of (a) SST (color shading; °C), sea surface wind (vectors; m s^{-1}), and SST gradient magnitude (contours; °C km^{-1}); (b) SST gradient magnitude (color shading), SST gradient vectors (red), and wind stress vectors (black); (c) wind stress divergence; and (d) wind stress curl. The contours overlaid in (c) and (d) denote SST, and magenta contours show the 200-m bathymetries in the northern South China Sea.

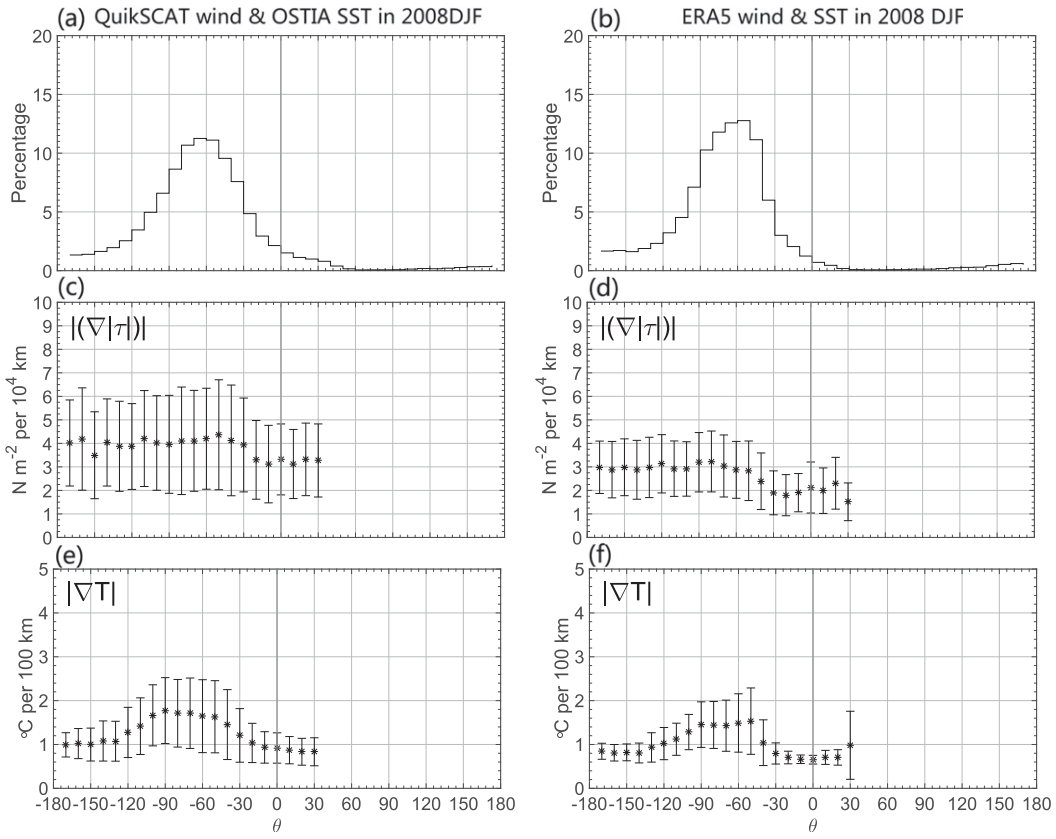

FIG. 3. Binned scatterplots of the angular dependencies of (a),(b) the number of observations, (c),(d) the magnitude of $\nabla|\boldsymbol{\tau}|$, and (e),(f) the magnitude of ∇T over the three months of data from December 2008 to February 2009. The abscissa is the counterclockwise angle θ from the SST gradient vector to the wind stress vector. The solid circles and vertical bars in (c)–(f) represent the mean and ± 1 standard deviation of the scatter of points within each bin. Bins larger than 30° are discarded in (c)–(f) due to the small number of grids shown in (a) and (b). (left) Plots of QuikSCAT wind and OSTIA SST, and (right) plots of ERA5 wind and SST.

difference in the spatial resolution. Furthermore, qualitatively similar responses of the surface stress and ENW to the SST are confirmed in the study of O'Neill et al. (2012). Therefore, SST–wind coupling is referred to as the wind stress response to the SST in this study.

The OSTIA SST and ERA5 data are linearly interpolated to the QuikSCAT grid for the calculation and analysis. It has been documented that orographic effects create wind stress mesoscale anomalies that are more intense than SST-induced anomalies in coastal regions (Boé et al. 2011; Renault et al. 2015). Nonetheless, after discarding the grids with an offshore distance of less than 25 km, QuikSCAT still provides robust data for the analysis of SST–wind coupling in the coastal sea of the NSCS.

The regridded daily satellite and reanalysis data are low-pass filtered using a 3-day running mean. For the three months of the boreal winter [1 December–28 February (DJF)], there are 88 pairs of data at one QuikSCAT grid for quantifying the responses of surface wind stress to the SST anomalies associated with the front. As shown later, the difference between satellite data and the reanalysis data for the coupling of wind and SST can be found in each of the DJFs from 2000 to 2019, indicating that one season of DJF data is sufficient to demonstrate the difference. Because the SST–wind coupling strength in DJF of 2008 is close to the mean strength of all the DJFs from 2000 to 2019, we mainly present the analysis results in DJF of 2008 in this study.

b. *Preprocessing for the surface wind stress and SST field*

Most previous studies investigating mesoscale SST–wind coupling in the frontal region have applied spatial high-pass filtering to isolate the mesoscale SST influence on surface winds. The same method is carried out in this study. A rectangular (3° × 2°) moving window is applied to obtain the spatially smoothed (low-pass) SST (T), wind stress ($\boldsymbol{\tau}$), and its deriving fields. Then, the mesoscale anomalies of a variable T' or $\boldsymbol{\tau}'$ are obtained by $T' = T - \overline{T}$, and $\boldsymbol{\tau}' = \boldsymbol{\tau} - \overline{\boldsymbol{\tau}}$, where the variables with overbars are the spatially smoothed fields and the dashed variables are the isolated spatial high-wavenumber perturbations.

The perturbation of angle θ is not directly calculated using the spatial-high-pass filter. It is assumed at first that positive SST–wind coupling is valid for the perturbations induced by the SST front; then, we should expect $\nabla \cdot \boldsymbol{\tau}'$ to vary linearly with $(\nabla T \cdot \hat{\boldsymbol{\tau}})'$ and $\nabla \times \boldsymbol{\tau}'$ to vary linearly with $(\nabla T \times \hat{\boldsymbol{\tau}})' \cdot \mathbf{k}$. This

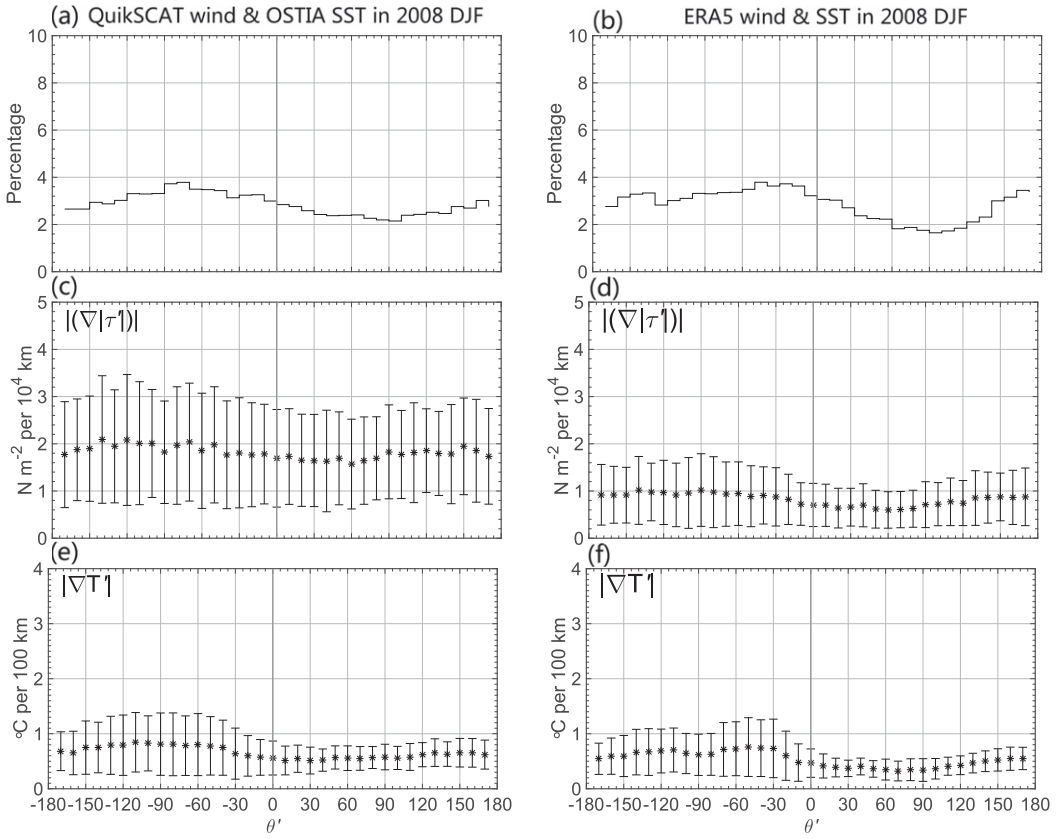

FIG. 4. As in Fig. 3, but for the perturbation wind stress fields and SST, τ', and T'. The abscissa is the perturbation counterclockwise angle θ' defined by Eq. (1).

means that $\nabla \cdot \boldsymbol{\tau}'$ and $\nabla \times \boldsymbol{\tau}'$ should be proportional to the cosine and sine of θ' defined as

$$\theta' = \tan^{-1}\left[\frac{(\nabla T \times \hat{\boldsymbol{\tau}})' \cdot \mathbf{k}}{(\nabla T \cdot \hat{\boldsymbol{\tau}})'}\right], \tag{1}$$

since the numerator and denominator in Eq. (1) can be written as

$$(\nabla T \cdot \hat{\boldsymbol{\tau}})' = |\nabla T'| \cos\theta', \quad \text{and} \tag{2}$$

$$(\nabla T \times \hat{\boldsymbol{\tau}})' \cdot \mathbf{k} = |\nabla T'| \sin\theta'. \tag{3}$$

The left sides of Eqs. (2) and (3) are directly calculated using the spatial-high-pass filter. Therefore, if the assumed SST–wind relations are proven, so is the definition of θ' (Chelton et al. 2001; O'Neill et al. 2005).

The spatial filter cutoff (3° × 2°) applied in this study is narrower in the meridional direction than in the zonal direction. This is because the coastal front in the NSCS is long but narrow. The south–north width of the front associated with a significant SST gradient is less than approximately 220 km in most areas (Fig. 2b). Therefore, the meridional scale of most mesoscale SST perturbations should be less than 220 km. Meanwhile, as evidenced in Liu et al. (2010), there are many SST perturbations induced by the meandering of the front, and the zonal scale of these perturbations is less than 100 km. Therefore, this filter cutoff is long enough to retain most mesoscale perturbations of wind and SST in the frontal area. On the other hand, this filter is short enough to reduce the biases of the spatial smoothing near the boundary due to the absence of data.

3. Response of the surface wind stress field to the SST front in the NSCS

a. *Mean state of surface wind stress and SST front*

A monthly average map of QuikSCAT wind and OSTIA SST for December 2008 is shown in Fig. 2a. It is a representative period of winter monsoon analyzed in the study area. During this period, the northeasterly monsoon covered the entire domain, and a southwest–northeast-oriented front was identified parallel to the coastline. The SST gradient is generally weaker in the western portion of the NSCS than in the eastern area near the Taiwan Strait. Visual examination suggests that coastal fronts mainly occur in three areas in the NSCS where the magnitude of the SST gradient exceeds 0.01°C km^{-1}, and it can be seen clearly that the wind stress is higher over warm water and lower over cold water. As summarized in the introduction, the close relationship between SST and wind stress magnitude is qualitatively consistent with the positive SST–wind coupling.

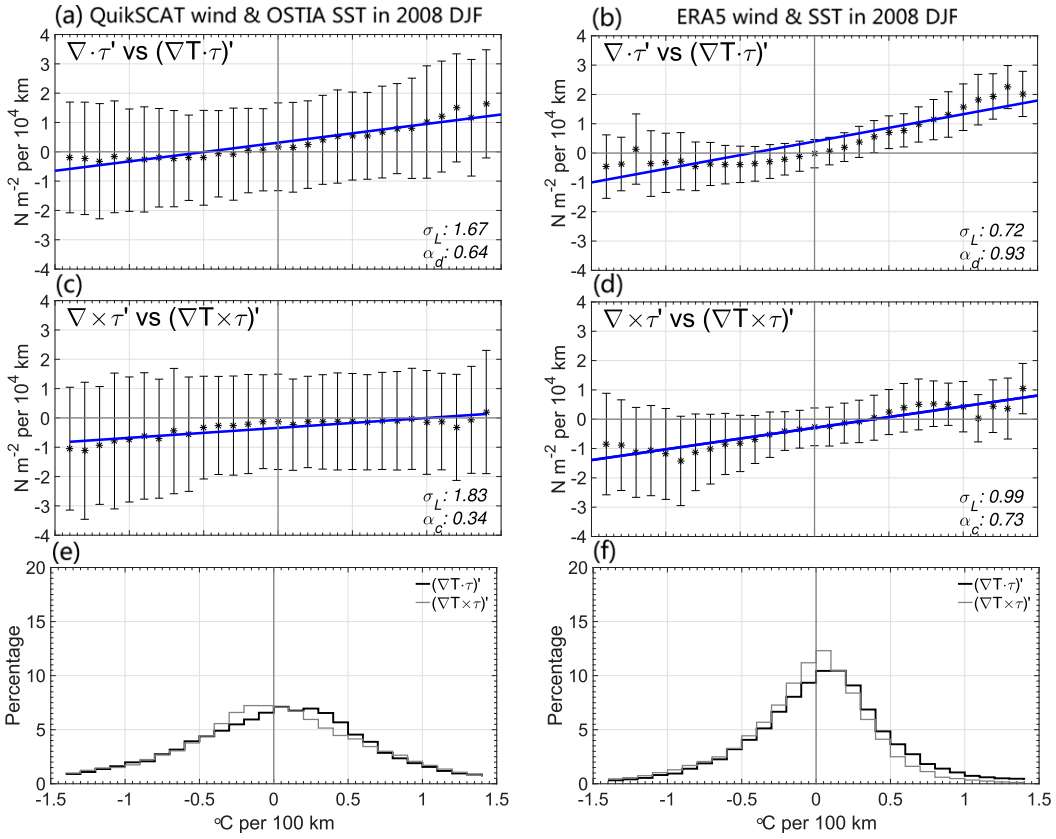

FIG. 5. Binned scatterplots of the relationships between spatial high-pass filtered SST and derived wind stress field: (a),(b) the perturbation wind stress divergence, $\nabla \cdot \boldsymbol{\tau}'$, plotted as a function of the perturbation downwind SST gradient $(\nabla T \cdot \hat{\boldsymbol{\tau}})'$; (c),(d) perturbation wind stress curl, $\nabla \times \boldsymbol{\tau}'$, plotted as a function of crosswind SST gradient $(\nabla T \times \hat{\boldsymbol{\tau}})'$; and (e),(f) histograms of the number of observations within each bin for (a) and (b). Here $\nabla \cdot \boldsymbol{\tau}'$ and $\nabla \times \boldsymbol{\tau}'$ are separated into 0.1°C 10^{-2} km^{-1} bins defined by the perturbation of crosswind or downwind SST gradients. The solid circles represent the overall mean values within each bin. The associated vertical bars represent the ±1 standard deviation of the mean values within each bin, and σ_L is the averaged standard deviation. The regression lines represent least squares fits of the binned overall means; α_d and α_c are defined in the text.

As shown in Fig. 2c, a band of high divergence is overlaid on the coastal SST front, where the wind stress increases as the airflow across isotherms moves toward warmer water. Two intense wind stress divergence bands are observed at the western NSCS and southwest off Taiwan, where strong SST gradients are marked by close SST contours. Meanwhile, a convergence zone is also observed south of the Taiwan Strait, where the SST contours are close. This convergence is caused by the narrowing effect of the strait, which intensifies the northeasterly monsoon inside the strait but weakens it out of the strait. Therefore, the surface winds in this area are strongly influenced by the topography and are excluded from our analysis.

The wind stress curl is negative in areas where the winds blow almost parallel to the isotherms over the frontal area (Fig. 2d). This pattern in the wind stress curl field develops because the winds are weaker over cold water but stronger over warm water to the south of the wind direction, resulting in a lateral change in the wind stress and negative wind stress curl. A dipole pattern of the surface wind stress curl, whose western boundary is located at approximately 119°E, is observed southwest of Taiwan (Fig. 2d). This feature of the wind stress curl is mainly caused by the influence of mountains on the northeasterly monsoon, which has been documented in other studies (Wang et al. 2008) and will not be further discussed in this study. Thus, the following analysis is carried out in the region west of 119°E, where there are 38 × 30 QuikSCAT grids.

b. *Response of surface wind stress to the SST front*

Figure 3 quantifies the relation between the divergence of surface wind stress, SST gradient, and angle θ in three months from December 2008 to February 2009 in the NSCS. QuikSCAT surface wind stress and OSTIA SST are analyzed first, referred to as satellite observations hereafter. As shown in Fig. 3a, angles θ are not fully sampled from −180° to 180°. One significant peak in the histogram of θ centered near $\theta = -60°$ indicates the observations within the frontal area where the surface wind blows to the southwest, and the SST gradient is primarily directed to the south and southeast (Fig. 2b). Meanwhile, there is no

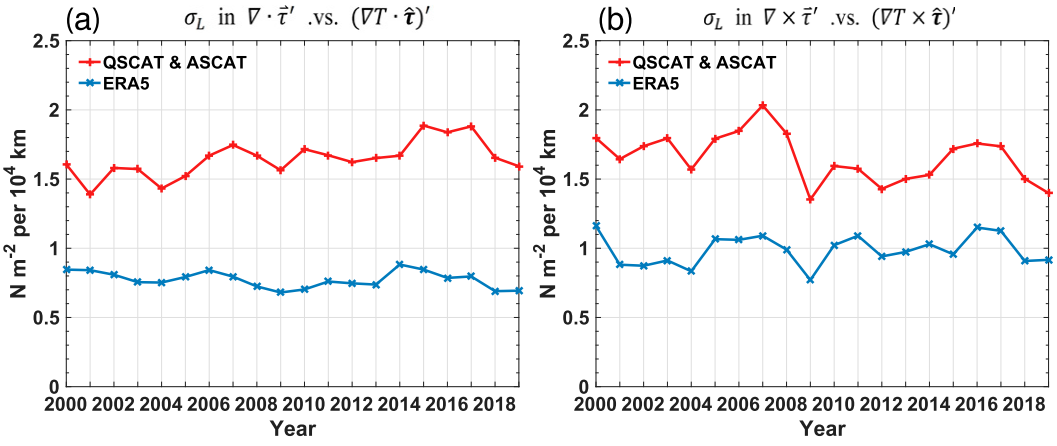

FIG. 6. Time series of the averaged standard deviation σ_L in the linear relationship (a) between $\nabla \cdot \boldsymbol{\tau}'$ and $(\nabla T \cdot \hat{\boldsymbol{\tau}})'$ and (b) between $\nabla \times \boldsymbol{\tau}'$ and $(\nabla T \times \hat{\boldsymbol{\tau}})'$ in all DJF periods from 2000 to 2019.

apparent peak in the histogram of $|(\nabla|\boldsymbol{\tau}|)|$, but a peak in the mean values of SST gradient ∇T is observed at $\theta = -90°$.

The composed ERA5 wind and SST results are also shown in Fig. 3, referred to as the reanalysis data hereafter. Compared to the satellite observations, there are some small differences in the histograms of the reanalysis data. For example, the number of samples seems to be more concentrated in the region from $\theta = -120°$ to $\theta = 0°$ (Fig. 3b). The magnitudes and the standard deviations of $\nabla|\boldsymbol{\tau}|$ are smaller in the ERA5 data than in the QuikSCAT observation. The ERA5 data described the peak of ∇T in the study area, but the magnitude of ∇T is smaller than that shown by the OSTIA SST.

The asymmetric distributions of θ and ∇T on the abscissa are removed using the spatial-high-pass filter to isolate the SST gradient and surface wind stress anomalies. As shown in Fig. 4, the distributions of θ', magnitudes of $\nabla|\boldsymbol{\tau}'|$, and $\nabla T'$ within each bin are much more nearly uniform than the unfiltered fields shown in Fig. 3. It is further confirmed that there is good agreement between the binned mean value of $\nabla \cdot \boldsymbol{\tau}'$ and $\nabla \times \boldsymbol{\tau}'$ and the sine and cosine fitting of θ', as we expected in the definition of Eq. (1). Therefore, the relationships between the derivative perturbation wind and the underlying perturbation SST gradient components are quantified in Fig. 5.

As shown in Figs. 5b and 5d, the ERA5 data confirm that the binned mean values of the perturbation wind stress divergence, $\nabla \cdot \boldsymbol{\tau}'$, vary linearly with the downwind perturbation SST gradient, $(\nabla T \cdot \hat{\boldsymbol{\tau}})'$, and the binned mean values of the perturbation wind stress curl, $\nabla \times \boldsymbol{\tau}'$, vary linearly with the crosswind perturbation SST gradient $(\nabla T \times \hat{\boldsymbol{\tau}})' \cdot \mathbf{k}$. The QuikSCAT wind and OSTIA SST also presented these linear relations in the binned scatterplots (Figs. 5a,c), but the slopes of the linear fitting lines were smaller than those of the ERA5 data.

The slope of the linear fitting line is defined as the coupling coefficient α, indicating the SST–wind coupling strength. The satellite observations show that the coupling coefficient between $\nabla \cdot \boldsymbol{\tau}'$ and $(\nabla T \cdot \hat{\boldsymbol{\tau}})'$, α_d, is $0.64 \times 10^{-2}\,\mathrm{N\,m^{-2}\,°C^{-1}}$ (Fig. 5a), which is approximately 2 times larger than the coupling coefficient between $\nabla \times \boldsymbol{\tau}' \cdot \mathbf{k}$ and $(\nabla T \times \hat{\boldsymbol{\tau}})' \cdot \mathbf{k}$, α_c (Fig. 5c). Meanwhile, the ERA5 data yield a value of $0.93 \times 10^{-2}\,\mathrm{N\,m^{-2}\,°C^{-1}}$ for α_d and $0.73\,\mathrm{N\,m^{-2}\,°C^{-1}}$ for α_c. The coupling strength α_c is approximately 30%–50% weaker than α_d, consistent with previous studies in other frontal regions at tropical and midlatitudes (O'Neill et al. 2010a). This indicates the different influences of SST gradient components on the derivative wind stress fields.

The satellite observations and reanalysis data confirm the linear relations between the derivative of $\boldsymbol{\tau}'$ and perturbation SST gradient components. However, there are pronounced differences in the coupling strength and the standard deviations of the binned scatterplots. It is shown that the coupling coefficients α_d and α_c are both smaller in the satellite observations than in the reanalysis data. Meanwhile, the averaged standard deviations within each bin, σ_L, are approximately 2 times larger in the satellite observations than in the reanalysis data. Such apparent differences in σ_L between the satellite observation and reanalysis data have not been reported in studies at other frontal regions.

Figure 5 shows that the SST–wind coupling strength is more substantial in the ERA5 data than in the satellite observations. This is a significant improvement in the ERA5 data since the previous study reported that the coupling coefficient obtained by the former ECMWF operational forecast model (T511) is approximately half as large as that of the QuikSCAT observations (Chelton 2005; Maloney and Chelton 2006). However, the noise of the SST–wind coupling is significant in the satellite observations, which could increase the biases of the coupling coefficients. Such noise is presented by the averaged standard deviations σ_L in the binned scatterplots. The source of this noise and its essential effect on the linear relations needs to be further clarified.

It is also necessary to examine whether the significant contrast in noise between satellite observations and reanalysis data in 2008 DJF is not a solitary case. The averaged standard deviations σ_L in the binned scatterplots are calculated for all the DJF periods from 2000 to 2019 (Fig. 6). There is no abrupt change in σ_L from year to year, and the differences between the σ_L of the satellite observations and reanalysis data are stable over the past 20 years. The σ_L of the satellite observations is always approximately 0.5 to $0.6\,\mathrm{N\,m^{-2}}$ per 10^4 km larger than the σ_L of the reanalysis data. Figure 6 suggests that the apparent difference in σ_L between satellite observations

TABLE 1. Statistical parameters of the linear regressions between $(\nabla \cdot \boldsymbol{\tau})'$ and $(\nabla T \cdot \hat{\boldsymbol{\tau}})'$ with different spatially smoothed satellite observations; σ_L is the averaged standard deviation; α_d is the slope of the linear regression between the wind stress divergence and downwind SST gradient; r is the correlation coefficient between the regression lines and the overall mean values within each bin; and R^2 is the R-square statistic of the linear regression. The values in parentheses are the results of ERA5 reanalysis data. Asterisks (*) mark the values calculated in the region $|(\nabla T \cdot \hat{\boldsymbol{\tau}})'| < 0.5 \times 10^{-2}$°C km^{-1} where the total percentage of the sample is more than 95%.

	Spatial smoothing window size							
	No smoothing	0.75° × 0°	0.75° × 0.75°	1.25° × 0°	1.25° × 0.75°	1.75° × 0.75°	1.25° × 1.25°	1.75° × 1.75°
σ_L	1.67 (0.72)	1.53	1.29	1.36	1.12	0.96	0.86	0.43*
α_d	0.64 (0.93)	0.89	0.96	0.89	1.07	1.18	1.01	1.79*
r	0.98 (0.98)	0.88	0.79	0.87	0.84	0.90	0.70	0.99*
R^2	0.97 (0.97)	0.78	0.62	0.77	0.71	0.81	0.51	0.98*

and reanalysis data in the DJF in 2008 is not a particular case but a common feature in the NSCS. In the following sections, our analysis focuses on DJF in 2008, but the results are also applicable for DJF in other years.

4. Effects of spatial scale modification on SST–wind coupling

a. *Influence of smoothed $\boldsymbol{\tau}$ and SST on the SST–wind coupling*

Figures 5 and 6 show that the noise in the linear relations between the derivative of perturbation wind stress and SST gradient is relatively large in the satellite observations. This noise is possibly related to the fine spatial structures of wind stress and SST in the satellite observations, although the resolutions of QuikSCAT and ERA5 wind are similar, as introduced in section 2a. Therefore, it is assumed that this noise should be depressed if presmoothing of the wind and SST fields is carried out before spatial-high-pass fitting.

Several sensitivity experiments are carried out to examine this hypothesis. In the sensitivity experiments, the original QuikSCAT wind and OSTIA SST are spatially smoothed by a moving window that is smaller than a spatial-high-pass filter. Then, the new spatial-high-pass perturbation fields and their derivatives are calculated using the smoothed data and applied to remake the binned scatterplots. Finally, the statistical characteristics of these new binned scatterplots are calculated and shown in Tables 1 and 2.

Table 1 shows the change in statistical parameters for the binned scatterplots between $\nabla \cdot \boldsymbol{\tau}'$ and $(\nabla T \cdot \hat{\boldsymbol{\tau}})'$. Generally, the noise in the linear relation is significantly reduced by increasing the smoothing window size. The averaged standard deviations σ_L decreased from 1.67 to 0.86 N m^{-2} per 10^4 km after the original satellite observations were smoothed by a window of 1.25° × 1.25°. Meanwhile, the coupling coefficient α_d increases from 0.64 to 1.01 N m^{-2} °C^{-1}. Nevertheless, the change in the confidence level and correlation coefficient is small. It is also noticed that the samples of binned scatterplots gradually concentrate in a region where $(\nabla T \cdot \hat{\boldsymbol{\tau}})' < 0.5 \times 10^{-2}$ °C km^{-1} due to the depression of extreme values by smoothing.

Table 2 shows the change in statistical parameters for the binned scatterplots between $\nabla \times \boldsymbol{\tau}'$ and $(\nabla T \times \hat{\boldsymbol{\tau}})' \cdot \mathbf{k}$. Similar to the results shown in Table 1, σ_L is also reduced by the growth of the smoothing window size. However, unlike α_d, the coupling coefficient α_c and the confidence level of the linear relationship both gradually decrease when the smoothing window size increases. Since the meridional length of the smoothing window gradually approaches the meridional length of the spatial-high-pass filter (3° × 2°), the perturbation fields are actually collected in a narrow band. Therefore, there is no significant linear relationship when a smoothing window of 1.75° × 1.75° was applied to the original satellite observations.

Tables 1 and 2 show that the spatial smoothing of QuikSCAT wind and OSTIA SST could significantly reduce the noise and change the coupling coefficients in the binned scatterplots. This is because spatial smoothing not only performs low-pass filtering of $\boldsymbol{\tau}$ but also depresses some spatial high-wavenumber perturbations of τ' and its derivative fields. The depressed spatial high-wavenumber perturbations of $\nabla \cdot \boldsymbol{\tau}'$ and $\nabla \times \boldsymbol{\tau}'$ may be the primary source of noise in the binned scatterplots of satellite observations. This issue is further discussed in the next section.

b. *The spatial frequency of $\nabla \cdot \boldsymbol{\tau}'$ in one transect*

Figure 7 shows the time–longitude distributions of $\nabla \cdot \boldsymbol{\tau}'$ along a zonal transect at 21.375°N. Figures 7a and 7b show robust perturbations of $\nabla \cdot \boldsymbol{\tau}'$ in both QuikSCAT observation

TABLE 2. As in Table 1, but for the linear regressions between $(\nabla \times \boldsymbol{\tau})' \cdot \mathbf{k}$ and $(\nabla T \times \hat{\boldsymbol{\tau}})' \cdot \mathbf{k}$. A dash (—) means no mathematical values are obtained.

	Spatial smoothing window size							
	No smoothing	0.75° × 0°	0.75° × 0.75°	1.25° × 0°	1.25° × 0.75°	1.75° × 0.75°	1.25° × 1.25°	1.75° × 1.75°
σ_L	1.83 (0.99)	1.71	1.43	1.49	1.19	1.03	1.04	0.27
α_c	0.34 (0.73)	0.67	0.55	0.57	0.19	0.09	0.09	—
r	0.92 (0.88)	0.88	0.71	0.78	0.28	0.17	0.17	—
R^2	0.86 (0.78)	0.78	0.51	0.61	0.08	0.03	0.03	0.03

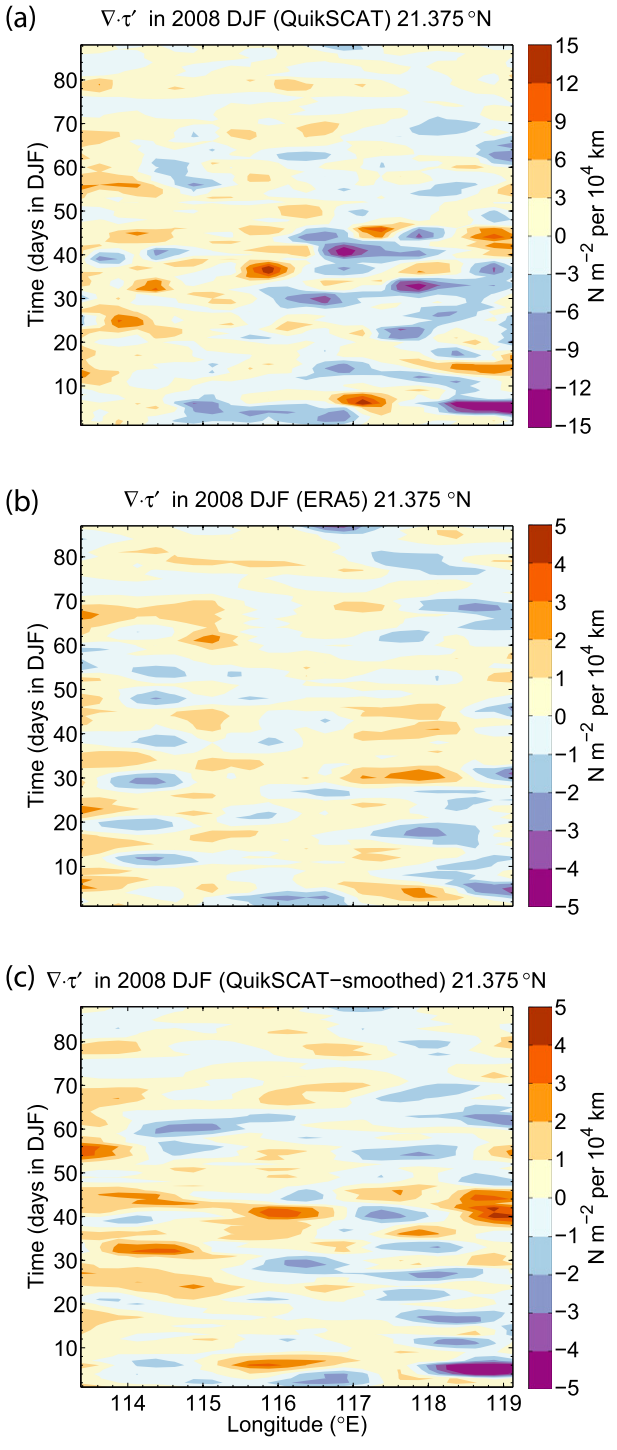

FIG. 7. Time–longitude distribution of $\nabla \cdot \boldsymbol{\tau}'$ in the zonal transect of 21.875°N for (a) QuikSCAT observations, (b) ERA5 data, and (c) the 1.25° × 1.25° spatially smoothed QuikSCAT observations.

and reanalysis data. Considering a pair of positive and negative values as one period for the variation of $\nabla \cdot \boldsymbol{\tau}'$, the horizontal distance of this pair approximately equals a length scale $1/\omega_s$, where ω_s is the spatial frequency of $\nabla \cdot \boldsymbol{\tau}'$ in the transect. From Fig. 7a, it can be seen that $1/\omega_s$ of most perturbations are approximately 100 km in the QuikSCAT observations. As a comparison, $1/\omega_s$ of most perturbations are longer than 100 km in the ERA5 data (Fig. 7b). Meanwhile, $1/\omega_s$ of the 1.25° × 1.25° smoothed QuikSCAT observation seems longer than 100 km, which is similar to the ERA5 data (Fig. 7c).

The length scale $1/\omega_s$ for the perturbations of $\nabla \cdot \boldsymbol{\tau}'$ is further quantified using wavelet analysis in this study. A zonal or meridional transect of $\nabla \cdot \boldsymbol{\tau}'$ in one day is connected with the same transect of $\nabla \cdot \boldsymbol{\tau}'$ in the day after. Then, a "time" series of $\nabla \cdot \boldsymbol{\tau}'$ is obtained by connecting the same transect over 88 days. This means that if there were n grids in the transect, there were $n \times 88$ points in the "time" series. The abscissa of the obtained power spectrum is a composition of space and time, and the vertical axis is the length scale $1/\omega_s$, which is the reciprocal of spatial frequency.

The power spectrum for the perturbations of $\nabla \cdot \boldsymbol{\tau}'$ at 21.375°N is shown in Fig. 8. Two major bands of $1/\omega_s$ in the QuikSCAT observations correspond to $1/\omega_s$ equaling approximately 90 and 190 km (Fig. 8a). Two significant perturbation bands are also confirmed on the power spectrum of ERA5 data but correspond to $1/\omega_s$ equaling approximately 75 km and 150 km, respectively (Fig. 8b). Moreover, the QuikSCAT observations show that the perturbations of $\nabla \cdot \boldsymbol{\tau}'$ are also significant in the region where $1/\omega_s$ is less than 75 km. As a comparison, these perturbations of $\nabla \cdot \boldsymbol{\tau}'$ are confirmed less frequently in the reanalysis data and were also significantly depressed by the spatial smoothing of QuikSCAT data (Fig. 8c). Figure 8 shows that when $1/\omega_s$ is less than 75 km, there are more perturbations of $\nabla \cdot \boldsymbol{\tau}'$ in the QuikSCAT observations than in the ERA5 data.

Figure 8 also shows that significant perturbations were not always observed throughout DJF but were occasionally observed. For example, most perturbations of $\nabla \cdot \boldsymbol{\tau}'$ were observed by QuikSCAT in December and January but almost disappeared in February (Fig. 8a). Although some perturbations of $\nabla \cdot \boldsymbol{\tau}'$ at $1/\omega_s$ equal to approximately 150 km could still be confirmed in February from the ERA5 data, the perturbations at $1/\omega_s$ equal to 75 km gradually weakened and disappeared (Fig. 8b). On the other hand, the observed lifetime of the perturbations varied with the change in $1/\omega_s$. Relatively large $1/\omega_s$ perturbations could be continuously observed for more than 5 days, whereas small $1/\omega_s$ perturbations usually dissipated in 2 or 3 days. The different preservation times could potentially change divergence and curl responses to the SST gradients.

c. *Spatial distribution of $1/\omega_s$ for $\nabla \cdot \boldsymbol{\tau}'$ and $\nabla \times \boldsymbol{\tau}'$ in the NSCS*

Figure 8 is only a snapshot of the spatial frequency of $\nabla \cdot \boldsymbol{\tau}'$ in one transect. The spatial distribution of the different frequencies needs to be examined across the whole NSCS. Then, wavelet analysis is applied for $\nabla \cdot \boldsymbol{\tau}'$ and $\nabla \times \boldsymbol{\tau}'$ in zonal and meridional transects with an interval of 0.25° across the whole study area. For each transect, the power of the perturbations at each length scale $1/\omega_s$ is summed during the study period. The obtained latitude and longitude for the $1/\omega_s$ power spectra of $\nabla \cdot \boldsymbol{\tau}'$ and $\nabla \times \boldsymbol{\tau}'$ are shown in Figs. 9 and 10, respectively.

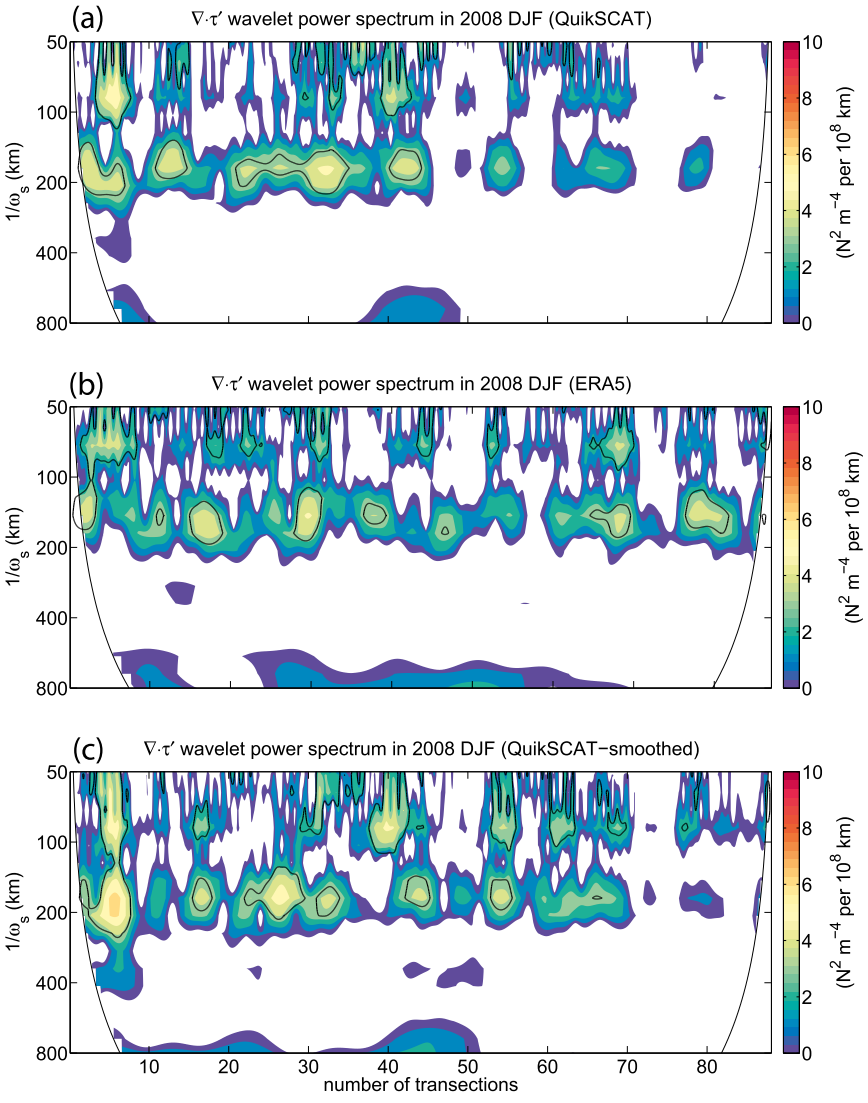

FIG. 8. Morlet wavelet power spectrum for the composed time series of $\nabla \cdot \boldsymbol{\tau}'$ at 21.875°N for (a) QuikSCAT observations, (b) ERA5 data, and (c) the 1.25° × 1.25° spatially smoothed QuikSCAT observations. The abscissa is a combination of the same longitude at 21.875°N over 88 days, and the vertical axis marks the length scale $1/\omega_s$ that is defined in section 4b. The black contours on the power spectra are at the 95% significance level.

Figure 9 shows an apparent difference between the satellite observation and reanalysis data for the spatial distribution of $1/\omega_s$ in $\nabla \cdot \boldsymbol{\tau}'$. In general, the power for the variance of $\nabla \cdot \boldsymbol{\tau}'$ is more energetic in the satellite observation than in the reanalysis data at the NSCS. Furthermore, the satellite observations show a wide range of $1/\omega_s$ from approximately 70 to 400 km for the zonal and meridional $\nabla \cdot \boldsymbol{\tau}'$ in the NSCS (Figs. 9a,c). However, the short $1/\omega_s$ perturbations ($1/\omega_s < 150$ km) of $\nabla \cdot \boldsymbol{\tau}'$ are not significant in the reanalysis data (Figs. 9b,d). Additionally, changes in significant $1/\omega_s$ in different areas are observed in the satellite data but are not clearly observed in the reanalysis data. For example, the short $1/\omega_s$ perturbations in the satellite observations are mainly confirmed south of 22°N and west of 116.5°E, and the long $1/\omega_s$ perturbations are much more significant north of 20°N and east of 116°E.

Figure 10 examines the spatial distribution of $1/\omega_s$ for the perturbation of $\nabla \times \boldsymbol{\tau}'$. Compared with Fig. 9, Fig. 10 shows a pronounced difference in the zonal perturbations of $\nabla \times \boldsymbol{\tau}'$. Although the total power of the perturbations is significant in satellite observation and reanalysis data, neither of them passed the 95% significance test (Figs. 10a,b). The perturbations of $\nabla \times \boldsymbol{\tau}'$ are mainly significant in the meridional direction in the study area (Figs. 10c,d). Similar to Fig. 9, for the scale of $1/\omega_s$ less than 100 km, the meridional perturbations are significant in the satellite observations but very weak in the reanalysis data. For the reanalysis data, the meridional perturbations of $\nabla \times \boldsymbol{\tau}'$ are mainly concentrated in the region of $1/\omega_s$ greater than 150 km (Fig. 10d). Nonetheless, both satellite observations and reanalysis data show that the power of long $1/\omega_s$ perturbations is

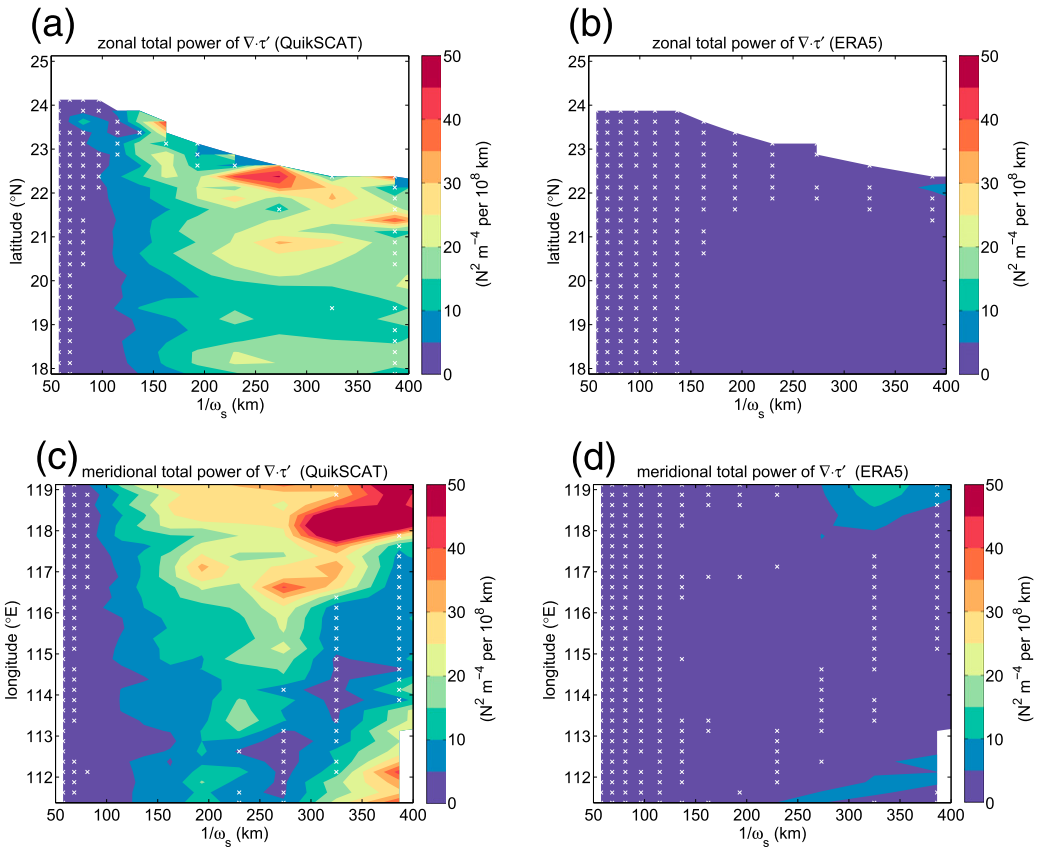

FIG. 9. Latitude–$1/\omega_s$ total power spectrum of $\nabla \cdot \boldsymbol{\tau}'$ for (a) QuikSCAT observation and (b) ERA5 reanalysis data and longitude–$1/\omega_s$ total power spectrum for (c) QuikSCAT observations and (d) ERA5 reanalysis data. Here, ω_s is the spatial frequency of $\nabla \cdot \boldsymbol{\tau}'$. The blank areas are where the obtained $1/\omega_s$ is longer than the number of valid QuikSCAT data grids. White crosses indicate that the power of variance does not pass the test of the 95% significance level.

much stronger in the eastern area than in the western area of the NSCS.

d. *The influence of different $1/\omega_s$ perturbations on the SST–wind coupling*

Figures 9 and 10 explicitly demonstrate that for the scale of $1/\omega_s$ less than 100 km, the satellite observations present more perturbations of $\nabla \cdot \boldsymbol{\tau}'$ and $\nabla \times \boldsymbol{\tau}'$ than the ERA5 reanalysis data. Moreover, these short $1/\omega_s$ perturbations could be crucial in determining the noise and coupling coefficients of the SST–wind coupling in the NSCS. Therefore, the coupling coefficients and the biases of the linear relationships are examined for the perturbations within different length scales. The length scale L is defined as $L = \sqrt{(1/\omega_{sx}^2) + (1/\omega_{sy}^2)}$, where ω_{sx} and ω_{sy} denote the zonal and meridional spatial frequencies of $\nabla \cdot \boldsymbol{\tau}'$ or $\nabla \times \boldsymbol{\tau}'$, respectively.

Figure 11a presents a pronounced unimodal structure in plotting the change in the coupling coefficients (linear regression slopes) within different L bands. The coupling coefficients α_d and α_d both increase at first and reach their maximum values when L is longer than approximately 200 km but smaller than approximately 300 km. Then, the coupling coefficients begin to decrease when L is larger than 300 km. This result emphasizes a critical scale range for the SST–wind coupling over the frontal area, and the linear relationship is significant in this range but declines outside of this range.

The coupling coefficient increase is accompanied by an apparent reduction in the noise (σ_L) in the linear relationship (Fig. 11b). When the length scale L increased from smaller than 50 km to larger than 100 km, σ_L was reduced by almost half by excluding the short L perturbations. In addition, the curvature showing the change in biases becomes gentle when the scale of perturbations becomes larger than approximately 200 km. This result proves that short L perturbations are the primary source of enormous noise in the linear relationships between SST and wind. In other words, the uncoupling feature of the SST and wind becomes significant when the perturbations are smaller than approximately 100 km in the study area.

It is worth noting that the sampling radius of the SST gradient components gradually shrinks when the wavelengths of the perturbations increase (Fig. 11c). The sampled maximum SST gradient perturbation $\nabla T'$ exceeds 0.9×10^{-2} °C km^{-1}

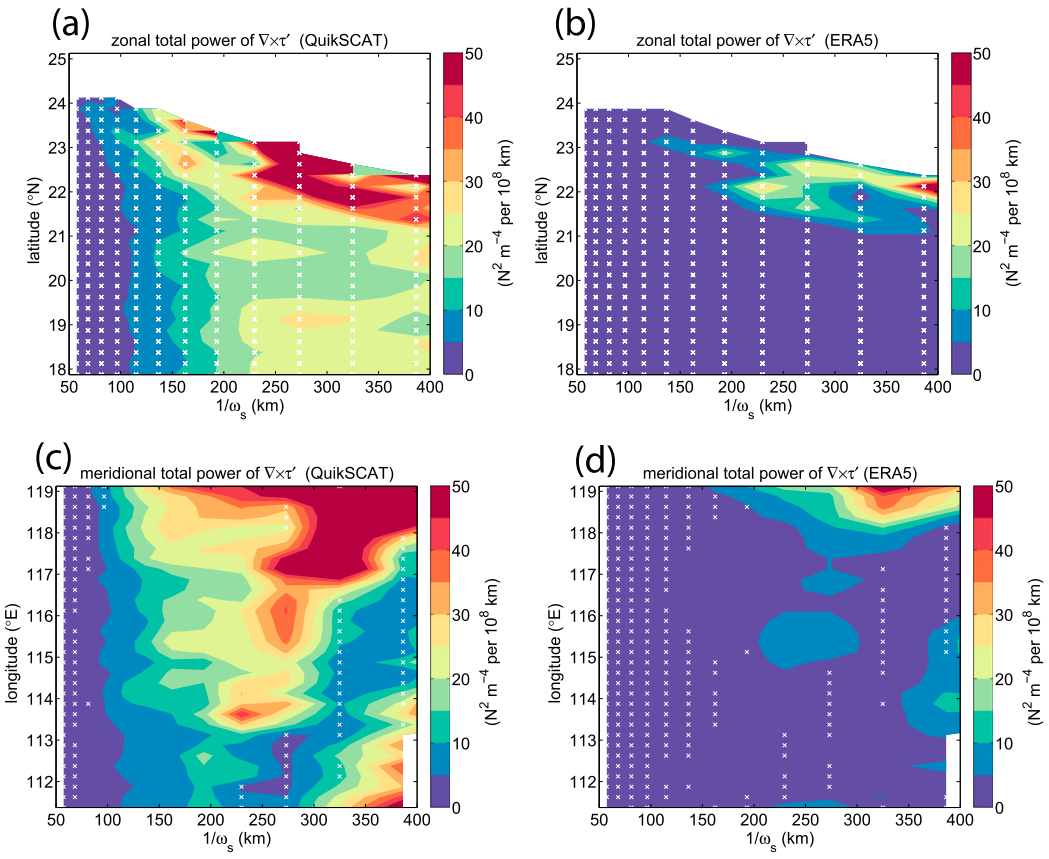

FIG. 10. As in Fig. 9, but for $\nabla \times \boldsymbol{\tau}'$.

when the length scale of the perturbations is smaller than approximately 50 km. The perturbation fields are sampled within the region where $|\nabla T'| \leq 0.3 \times 10^{-3}$ °C km^{-1} when L is broader than approximately 200 km, while the coupling coefficient reaches its maximum value. According to these results, the optimal wavelength-band filter for investigating the responses of the derivative wind stress field to the mesoscale SST anomalies can be decided.

Figure 12 shows the binned scatterplots for the bandpass filtered perturbations. The wavelength of the perturbations is longer than approximately 100 km but smaller than approximately 300 km. The noise σ_L of the linear relation between $\nabla \cdot \boldsymbol{\tau}'$ and $(\nabla T \cdot \hat{\boldsymbol{\tau}})'$ decreased by approximately 40% from ±1.67 in Fig. 5a to ±0.96 N m^{-2} in Fig. 12a, while the coupling coefficient α_d increased from 0.64×10^{-2} to 1.33×10^{-2} N m^{-2} °C^{-1}. The noise of the linear relation between $\nabla \times \boldsymbol{\tau}'$ and $(\nabla T \times \hat{\boldsymbol{\tau}})' \cdot \mathbf{k}$ decreased from ±1.83 to ±1.06 N m^{-2}, and the coupling coefficient α_c increased from 0.34×10^{-2} to 0.95×10^{-2} N m^{-2} °C^{-1}. Bandpass filtering between 100 and 300 km avoids losing too many perturbations in the frontal area and gives reasonable and general coupling features between the derivative wind stress and SST gradient components in the NSCS.

A possible explanation is discussed here for the dependence of SST–wind coupling on the spatial frequencies. According to Small et al. (2008) and Byrne et al. (2015), there are four length scales whose values help us to determine which process dominates the response of surface wind to SST perturbations. The four length scales are the cross-front length scale (L_f), the length scale on which the Coriolis term changes ($L_c = U/f$), the length scale over which the pressure gradient changes ($L_p = Uh^2/K_T$), and the length scale responsible for the vertical mixing of momentum ($L_m = Uh^2/K_m$). Here, U is the wind speed, h is the boundary layer height, and K_T and K_m denote the vertical eddy diffusion coefficient for air temperature and vertical eddy viscosity coefficient for momentum, respectively.

In this study, the average wind speed $U \geq 10$ m s^{-1} (Fig. 2a), boundary layer height $h \approx 1000$ m, $f \approx 0.5 \times 10^{-4}$ m s^{-1}, and $K_T \approx K_m \approx$ 50–100 m^2 s^{-1}. Therefore, L_c has an order of 200 km; L_p and L_m have an order of 100 km, which are all longer than the length scale of high wavenumber SST perturbations ($L_f \leq 50$ km). In this case, when an air column moves over the SST perturbations, the moving distance is not long enough for either the adjustment of the pressure gradient or the vertical diffusion of momentum to change the surface wind. Consequently, the positive SST–wind coupling is weak, and the noise in the linear relationship fitting is significant for ($L_f < L_p \sim L_m$).

On the other hand, when the length scale of SST perturbations is larger than 100 km ($L_f > 100$ km), the moving distance of the air column is long enough to allow the adjustment of the pressure gradient and the vertical diffusion of momentum to

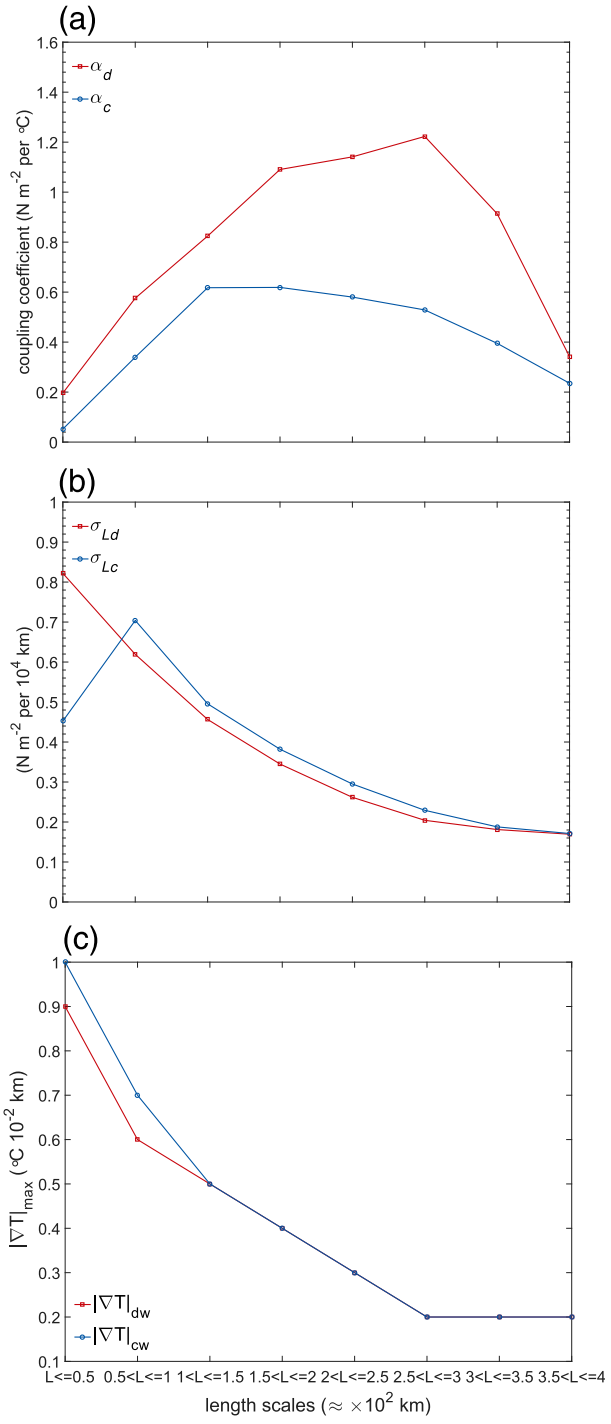

FIG. 11. The (a) coupling coefficients α, (b) averaged standard deviations σ_L, and (c) maximum SST gradient of the linear relationships between the perturbation fields calculated in different wavelength bands. The definition of L is given in section 4d. The subscripts d and c denote the variables obtained from the perturbation wind stress divergence and wind stress curl. The maximum downwind (∇T_{dw}) and crosswind (∇T_{cw}) SST gradient perturbations in (c) define the region within which the total percentage of the sample is more than 95%.

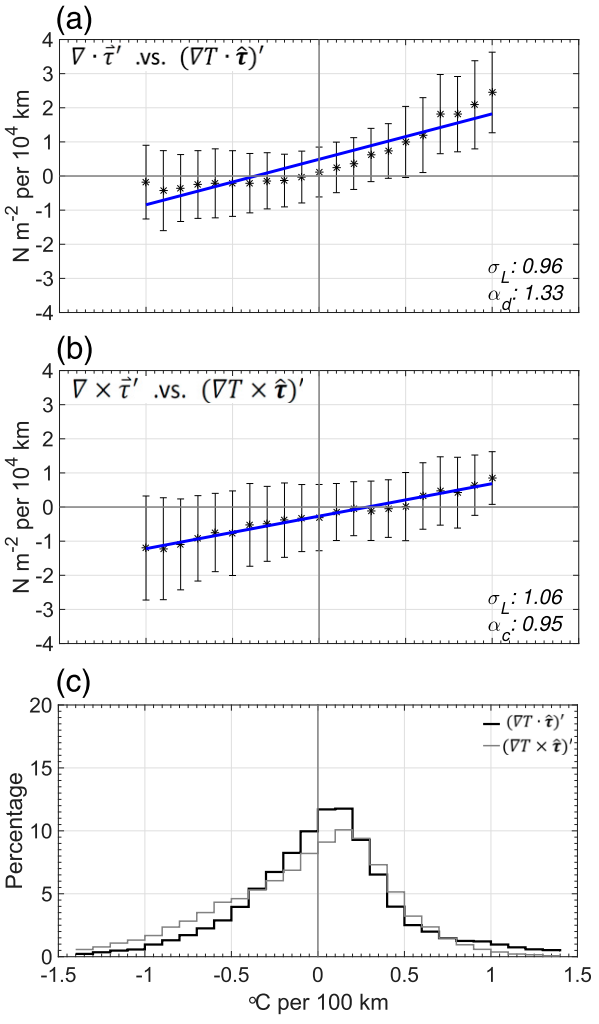

FIG. 12. Binned scatterplots of the relationships between the wavelength bandpass filtered field and (a) the perturbation wind stress divergence and the perturbation downwind SST gradient and (b) perturbation wind stress curl and crosswind SST gradient; (c) histograms of the number of observations within each bin for (a) and (b). The wavelength band for the spatial perturbations is 100 km $\leq L \leq$ 300 km.

change the surface wind. Therefore, the noise in the linear relationship fitting weakens, and the positive SST–wind coupling becomes significant (Fig. 11a). When the moving distance becomes larger than 300 km, the large-scale adjustments of the ocean and atmosphere become more significant than the influence of the SST front on the surface wind fields. Then, the positive SST–wind coupling weakens again (Fig. 11a).

5. Conclusions

The QuikSCAT observations of surface wind stress and OSTIA SST during the three months from 1 December 2008 to 28 February 2009 are analyzed to study the regional ocean–atmosphere coupling associated with the SST front in the northern South China Sea. The perturbation wind stress

vorticity and divergence are linearly related to the perturbation crosswind and downwind components of the SST gradient. However, the satellite observations show significant noise in the linear relationships, as represented by the standard deviations in the binned scatterplots.

The ERA5 reanalysis data are analyzed and compared with the satellite observations. The ERA5 reanalysis data gave satisfactory performance in describing the response of surface wind stress over the frontal area in the NSCS. The linear relationship between the derivative fields of perturbation wind stress and SST gradient components is even more substantial in the ERA5 data than in the satellite observations. Additionally, the noise in the linear relationships, as represented by the standard deviations in the binned scatterplots, is much smaller in the ERA5 data than in the satellite observations.

The apparent differences in the noise observed in the satellite observations and reanalysis data are rarely reported in other frontal areas. The sensitivity experiments show that spatial smoothing of satellite observations could significantly reduce the noise and change the coupling coefficients. This indicates that some specific high wavenumber perturbations depressed by spatial smoothing are crucial in investigating the SST–wind coupling in the NSCS. Then, a length scale $1/\omega_s$ (km) is defined to study the influences of perturbations with different wavenumbers (ω_s) on the noise in the linear relationships.

The $1/\omega_s$ length scales for the spatial variation in wind are obtained using wavelet analysis. The results show that the satellite scatterometer observed many perturbations at the length scale of $1/\omega_s < 100$ km in the NSCS. However, the perturbations at this scale were relatively weak in the ERA5 reanalysis data. The robust SST gradient at the length scale of $1/\omega_s < 100$ km does not lead to the corresponding linear responses in derivative wind stress but contributes to over 40% of the noise in the linear relations observed by QuikSCAT.

It is further found that the linear relations between surface vorticity and divergence in the crosswind and downwind SST gradients are significant when the mesoscale perturbations are larger than approximately 100 km but smaller than approximately 300 km in the NSCS. Spatial bandpass filtering between 100 and 300 km yields values for the coupling coefficients α_d and α_c of 1.33×10^{-2} and 0.95×10^{-2} N m^{-2} °C^{-1} in 2008 DJF, respectively. These values are reasonable and confident estimates compared to other frontal areas' results. Additionally, the coupling coefficient α_c is approximately 30% weaker than α_d, which is also consistent with previous studies based on observations and numerical simulations (O'Neill et al. 2010a).

The evaluation on four dynamical length scales shows that a distance of 100 km is the shortest distance that allows the pressure gradient and the vertical diffusion of momentum to adjust the surface wind in the NSCS. When the moving distance of an air mass over the front is less than 100 km, the adjustment of the pressure gradient and the vertical diffusion of momentum are insufficient to maintain stable positive SST–wind coupling. Thus, the noise in the linear relationship fitting is large. On the other hand, when the moving distance is larger than 100 km, positive SST–wind coupling is maintained by the combined effect of the pressure gradient and vertical mixing of momentum.

Distinguishing the dependencies of SST–wind coupling on spatial scales is the foundation of ongoing work. Although the year-to-year variability in the noise is small in the observations of QuikSCAT, there is an apparent change in the coupling strength. An accurate calculation of the coupling strength is fundamental for this work. On the other hand, as introduced in the introduction, the feedback of SST-induced mesoscale wind stress variability on the ocean is significant. This result may be used to study the effects of local mesoscale wind stress variability on the fine structure of the coastal front itself.

Acknowledgments. This research was supported by the Frontier Science Research Project of Chinese Academy of Sciences (Grant QYZDJ-SSW-DQC022), the Key Special Project for Introduced Talents Team of Southern Marine Science and Engineering Guangdong Laboratory (Guangzhou) (GML2019ZD0304), the Science and Technology Planning Project of Guangzhou City, China (202002030490 and 202102080363, the National Natural Science Foundation of China (Grants 41676018, 41521005, 41806035, 42076209, 41776025, and 41876017), and the Ministry of Education, Culture, Sports, Science and Technology, Japan (MEXT) to a project on Joint Usage/Research Center-Leading Academia in Marine and Environment Pollution Research (LaMer), the Rising Star Foundation of the South China Sea Institute of Oceanology (NHXX2019WL0101). The authors thank the High-Performance Computing Division of the South China Sea Institute of Oceanology for the support.

Data availability statement. All data used in this study are available at https://www.ecmwf.int/en/forecasts/datasets/reanalysis-datasets/era5 and https://apps.ecmwf.int/datasets/data/interim-full-daily/levtype=sfc/ for ERA5 reanalysis data, https://ghrsst-pp.metoffice.gov.uk/ostia-website/index.html for OSTIA SST, and http://apdrc.soest.hawaii.edu/data/data.php?discipline_index=3 for QuikSCAT and ASCAT wind.

REFERENCES

Boé, J., A. Hall, F. Colas, J. C. McWilliams, X. Qu, J. Kurian, and S. B. Kapnick, 2011: What shapes mesoscale wind anomalies in coastal upwelling zones? *Climate Dyn.*, **36**, 2037–2049, https://doi.org/10.1007/s00382-011-1058-5.

Byrne, D., L. Papritz, I. Frenger, and M. Münnich, 2015: Atmospheric response to mesoscale sea surface temperature anomalies: Assessment of mechanisms and coupling strength in a high resolution coupled model over the South Atlantic. *J. Atmos. Sci.*, **72**, 1872–1890, https://doi.org/10.1175/JAS-D-14-0195.1.

Chelton, D. B., 2005: The impact of SST specification on ECMWF surface wind stress fields in the eastern tropical Pacific. *J. Climate*, **18**, 530–550, https://doi.org/10.1175/JCLI-3275.1.

——, and S.-P. Xie, 2010: Coupled ocean–atmosphere interaction at oceanic mesoscales. *Oceanography*, **23**, 52–69, https://doi.org/10.5670/oceanog.2010.05.

——, and Coauthors, 2001: Observations of coupling between surface wind stress and sea surface temperature in the eastern

tropical Pacific. *J. Climate*, **14**, 1479–1498, https://doi.org/10.1175/1520-0442(2001)014<1479:OOCBSW>2.0.CO;2.

Chow, C. H., and Q. Liu, 2012: Eddy effects on sea surface temperature and sea surface wind in the continental slope region of the northern South China Sea. *Geophys. Res. Lett.*, **39**, L02601, https://doi.org/10.1029/2011GL050230.

Chu, P. C., and G. H. Wang, 2003: Seasonal variability of thermohaline front in the central South China Sea. *J. Oceanol.*, **59**, 65–78, https://doi.org/10.1023/A:1022868407012.

Dong, J., and Y. Zhong, 2020: Submesoscale fronts observed by satellites over the northern South China Sea shelf. *Dyn. Atmos. Oceans*, **91**, 101161, https://doi.org/10.1016/j.dynatmoce.2020.101161.

Gaube, P., D. B. Chelton, R. M. Samelson, M. G. Schlax, and L. W. O'Neill, 2015: Satellite observations of mesoscale eddy-induced Ekman pumping. *J. Phys. Oceanogr.*, **45**, 104–132, https://doi.org/10.1175/JPO-D-14-0032.1.

Hayes, S. P., M. J. McPhaden, and J. M. Wallace, 1989: The influence of sea surface temperature on surface wind in the eastern equatorial Pacific: Weekly to monthly variability. *J. Climate*, **2**, 1500–1506, https://doi.org/10.1175/1520-0442(1989)002<1500:TIOSST>2.0.CO;2.

Hersbach, H., and Coauthors, 2019: Global reanalysis: Goodbye ERA-Interim, hello ERA5. *ECMWF Newsletter*, No. 159, ECMWF, Reading, United Kingdom, 17–24, https://www.ecmwf.int/node/19027.

Hirahara, S., M. A. Balmaseda, E. de Boisseson, and H. Hersbach, 2016: Sea surface temperature and sea ice concentration for ERA5. ECMWF ERA Rep. Series 26, 25 pp., https://www.ecmwf.int/node/16555.

Hu, J., and X. H. Wang, 2016: Progress on upwelling studies in the China seas. *Rev. Geophys.*, **54**, 653–673, https://doi.org/10.1002/2015RG000505.

Koseki, S., and M. Watanabe, 2010: Atmospheric boundary layer response to mesoscale SST anomalies in the Kuroshio Extension. *J. Climate*, **23**, 2492–2507, https://doi.org/10.1175/2009JCLI2915.1.

Kuwano-Yoshida, A., and S. Minobe, 2017: Storm-track response to SST fronts in the northwestern Pacific region in an AGCM. *J. Climate*, **30**, 1081–1102, https://doi.org/10.1175/JCLI-D-16-0331.1.

Lindzen, R., and S. Nigam, 1987: On the role of sea surface temperature gradients in forcing low-level winds and convergence in the tropics. *J. Atmos. Sci.*, **44**, 2418–2436, https://doi.org/10.1175/1520-0469(1987)044<2418:OTROSS>2.0.CO;2.

Liu, S. M., X. Guo, Q. Chen, J. Zhang, Y. F. Bi, X. Luo, and J. B. Li, 2010: Nutrient dynamics in the winter thermohaline frontal zone of the northern shelf region of the South China Sea. *J. Geophys. Res.*, **115**, C11020, https://doi.org/10.1029/2009JC005951.

Maloney, E. D., and D. B. Chelton, 2006: An assessment of the sea surface temperature influence on surface wind stress in numerical weather prediction and climate models. *J. Climate*, **19**, 2743–2762, https://doi.org/10.1175/JCLI3728.1.

Minobe, S., A. Kuwano-Yoshida, N. Komori, S.-P. Xie, and R. J. Small, 2008: Influence of the Gulf Stream on the troposphere. *Nature*, **452**, U206–U251, https://doi.org/10.1038/nature06690.

Nakamura, H., A. Nishina, and S. Minobe, 2012: Response of storm tracks to bimodal Kuroshio path states south of Japan. *J. Climate*, **25**, 7772–7779, https://doi.org/10.1175/JCLI-D-12-00326.1.

Oerder, V., F. Colas, V. Echevin, S. Masson, and F. Lemarié, 2016: Mesoscale SST–wind stress coupling in the Peru–Chile current system: Which mechanisms drive its seasonal variability? *Climate Dyn.*, **47**, 2309–2330, https://doi.org/10.1007/s00382-015-2965-7.

O'Neill, L. W., D. B. Chelton, S. K. Esbensen, and F. J. Wentz, 2005: High-resolution satellite measurements of the atmospheric boundary layer response to SST variations along the Agulhas Return Current. *J. Climate*, **18**, 2706–2723, https://doi.org/10.1175/JCLI3415.1.

——, ——, and ——, 2010a: The effects of SST-induced surface wind speed and direction gradients on midlatitude surface vorticity and divergence. *J. Climate*, **23**, 255–281, https://doi.org/10.1175/2009JCLI2613.1.

——, S. K. Esbensen, N. Thum, R. M. Samelson, and D. B. Chelton, 2010b: Dynamical analysis of the boundary layer and surface wind responses to mesoscale SST perturbations. *J. Climate*, **23**, 559–581, https://doi.org/10.1175/2009JCLI2662.1.

——, D. B. Chelton, and S. K. Esbensen, 2012: Covariability of surface wind and stress responses to sea surface temperature fronts. *J. Climate*, **25**, 5916–5942, https://doi.org/10.1175/JCLI-D-11-00230.1.

——, T. Haack, D. B. Chelton, and E. Skyllingstad, 2017: The Gulf Stream convergence zone in the time-mean winds. *J. Atmos. Sci.*, **74**, 2383–2412, https://doi.org/10.1175/JAS-D-16-0213.1.

Perlin, N., S. P. de Szoeke, D. B. Chelton, R. M. Samelson, E. D. Skyllingstad, and L. W. O'Neill, 2014: Modeling the atmospheric boundary layer wind response to mesoscale sea surface temperature perturbations. *Mon. Wea. Rev.*, **142**, 4284–4307, https://doi.org/10.1175/MWR-D-13-00332.1.

Renault, L., A. Hall, and J. C. McWilliams, 2015: Orographic shaping of US West Coast wind profiles during the upwelling season. *Climate Dyn.*, **46**, 273–289, https://doi.org/10.1007/s00382-015-2583-4.

Samelson, R. M., E. D. Skyllingstad, D. B. Chelton, S. K. Esbensen, L. W. O'Neill, and N. Thum, 2006: On the coupling of wind stress and sea surface temperature. *J. Climate*, **19**, 1557–1566, https://doi.org/10.1175/JCLI3682.1.

Seo, H., A. J. Miller, and J. O. Roads, 2007: The Scripps Coupled Ocean–Atmosphere Regional (SCOAR) model, with applications in the eastern Pacific sector. *J. Climate*, **20**, 381–402, https://doi.org/10.1175/JCLI4016.1.

Shao, M., and Coauthors, 2019: The variability of winds and fluxes observed near submesoscale fronts. *J. Geophys. Res. Oceans*, **124**, 7756–7780, https://doi.org/10.1029/2019JC015236.

Shi, R., X.-Y. Guo, D. Wang, L. Zeng, and J. Chen, 2015: Seasonal variability in coastal fronts and its influence on sea surface wind in the northern South China Sea. *Deep-Sea Res. II*, **119**, 30–39, https://doi.org/10.1016/j.dsr2.2013.12.018.

——, and Coauthors, 2017: Ship observations and numerical simulation of the marine atmospheric boundary layer over the spring oceanic front in the northwestern South China Sea. *J. Geophys. Res. Atmos.*, **122**, 3733–3753, https://doi.org/10.1002/2016JD026071.

——, Q. Cai, L. Dong, X. Guo, and D. Wang, 2019: Response of the diurnal cycle of summer rainfall to large-scale circulation and coastal upwelling at Hainan, South China. *J. Geophys. Res. Atmos.*, **124**, 3702–3725, https://doi.org/10.1029/2018JD029528.

Skyllingstad, E. D., D. Vickers, L. Mahrt, and R. Samelson, 2007: Effects of mesoscale sea-surface temperature fronts on the marine atmospheric boundary layer. *Bound.-Layer Meteor.*, **123**, 219–237, https://doi.org/10.1007/s10546-006-9127-8.

——, S. P. de Szoeke, and L. W. O'Neill, 2019: Modeling the transient response of tropical convection to mesoscale SST

variations. *J. Atmos. Sci.*, **76**, 1227–1244, https://doi.org/10.1175/JAS-D-18-0079.1.

Small, R. J., S. P. Xie, L. W. O'Neill, H. Seo, Q. Song, P. Cornillon, M. Spall, and S. Minobe, 2008: Air–sea interaction over ocean fronts and eddies. *Dyn. Atmos. Oceans*, **45**, 274–319, https://doi.org/10.1016/j.dynatmoce.2008.01.001.

Spall, M. A., 2007: Midlatitude wind stress–sea surface temperature coupling in the vicinity of oceanic fronts. *J. Climate*, **20**, 3785–3801, https://doi.org/10.1175/JCLI4234.1.

Tokinaga, H., and Coauthors, 2006: Atmospheric sounding over the winter Kuroshio Extension: Effect of surface stability on atmospheric boundary layer structure. *Geophys. Res. Lett.*, **33**, L04703, https://doi.org/10.1029/2005GL025102.

Toy, M. D., and R. H. Johnson, 2014: The influence of an SST front on a heavy rainfall event over coastal Taiwan during TiMREX. *J. Atmos. Sci.*, **71**, 3223–3249, https://doi.org/10.1175/JAS-D-13-0338.1.

Wallace, J. M., T. P. Mitchell, and C. Deser, 1989: The influence of sea surface temperature on surface wind in the eastern equatorial Pacific: Seasonal and interannual variability. *J. Climate*, **2**, 1492–1499, https://doi.org/10.1175/1520-0442(1989)002<1492:TIOSST>2.0.CO;2.

Wang, D., Y. Liu, Y. Qi, and P. Shi, 2001: Seasonal variability of thermal fronts in the northern South China Sea from satellite data. *Geophys. Res. Lett.*, **28**, 3963–3966, https://doi.org/10.1029/2001GL013306.

Wang, G., D. Chen, and J. Su, 2008: Winter eddy genesis in the eastern South China Sea due to orographic wind jets. *J. Phys. Oceanogr.*, **38**, 726–732, https://doi.org/10.1175/2007JPO3868.1.

——, J. Li, C. Wang, and Y. Yan, 2012: Interactions among the winter monsoon, ocean eddy and ocean thermal front in the South China Sea. *J. Geophys. Res. Oceans*, **117**, C08002, https://doi.org/10.1029/2012JC008007.